PHYSICAL REVIEW D **107,** 075012 (2023)

Muon $g-2$ in a type-X 2HDM assisted by inert scalars: A test at the LHC

Nabarun Chakrabarty[*]

Department of Physics, Indian Institute of Technology Kanpur, Kanpur-208016, Uttar Pradesh, India

(Received 1 January 2023; accepted 16 February 2023; published 14 April 2023)

A scenario augmenting the well-known type-X two-Higgs doublet model with an additional inert doublet is proposed. The type-X two-Higgs doublet model is known to offer a solution to the muon $g-2$ anomaly for a light pseudoscalar. We show that the proposed framework can accommodate a heavier pseudoscalar on account of two-loop Barr-Zee contributions to muon $g-2$ stemming from the inert doublet. We subsequently explore an interesting $\tau^+\tau^-+$ missing transverse energy signal that can be used to probe the present scenario at the 14 TeV LHC.

DOI: 10.1103/PhysRevD.107.075012

I. INTRODUCTION

One of the experimental findings that continues to advocate dynamics beyond the Standard Model (SM) of particle physics is the longstanding muon $g-2$ anomaly. In a nutshell, a discrepancy has been noted between the SM prediction of the anomalous magnetic moment of the muon [1–11] and its experimental measurements made at BNL [12] and FNAL [13,14]. The combined excess reported is

$$\Delta a_\mu \equiv a_\mu^{\rm exp} - a_\mu^{\rm SM} = 251(59)\times 10^{-11}. \tag{1}$$

A minimal extension of the SM long known to resolve the muon $g-2$ anomaly is the type-X two-Higgs doublet model (2HDM) [15,16]. The model comprises an additional $SU(2)_L$ scalar doublet over and above SM. This entails an enlarged scalar sector, i.e., two CP-even neutral scalars h, H, a CP-odd neutral scalar A and a charged scalar H^+. A governing $\mathbb{Z}_2$ keeps the flavor changing neutral current at bay by demanding that a particular fermion interacts with only one of the two doublets. This leads to several variants and one such is the type-X 2HDM [16]. One important feature of the type-X is that quark Yukawa couplings involving the additional scalars are suppressed while the leptonic Yukawas are enhanced. It is the enhanced leptonic couplings that potentially give rise to sizeable muon $g-2$ contributions at the one-loop and two-loop levels. A resolution of the anomaly thus becomes possible for a light pseudoscalar ($M_A \lesssim 100$ GeV) and high $\tan\beta$ ($\tan\beta \gtrsim 20$) [17–25]. As a perk, by virtue of the small quark couplings, such a parameter region in the type-X evades stringent constraints from flavor observables and direct search from the colliders [26], especially the Large Hadron Collider (LHC). However, recent LHC searches for $h_{125} \to AA \to 4\tau, 2\tau 2\mu$ channels have disfavored a large $\mathrm{BR}(h_{125} \to AA)$ [27]. This strongly constrains the $M_A <$ 62.5 GeV parameter region. Furthermore, the large $\tan\beta$ region also get restricted by lepton precision observables. A partial list of collider probes of the type-X 2HDM is [28–34].

In this study, we seek to alleviate the aforementioned shortcoming by extending the scalar sector of the type-X 2HDM so that additional two-loop Barr-Zee (BZ) contributions are encountered.[1] The simplest multiplets leading to additional BZ diagrams are $SU(2)_L$ singlets with $Y \neq 0$. For instance, let us look more closely at the $Y=1$ case that is basically a singly charged scalar. This scalar can mix with the like-charge states in the 2HDM through the scalar potential and therefore can be searched at a collider via the $k^+ \to \ell^+\nu$. Here, k^+ refers to the charged scalar and $\ell = e$, μ, τ. While this is enticing, the scope to directly look for the scalar via the invariant mass handle is obviated owing to the presence of the neutrino(s). As for an $SU(2)_L$-singlet $Y \geq 2$ scalar (that is, $Q \geq 2$), there would be no mixing of the same with the 2HDM sector that features neutral and singly charged scalars only. Such a case therefore will also not be attractive from the collider perspective. Neutral scalars offer the possibility of having opposite-sign lepton final states at a collider. Thus, while we postulate the existence of charged scalars to induce BZ diagrams, we also aim to probe such a framework via decays of neutral scalars. And the lowest multiplet that features both charged and neutral scalars is $(\mathbf{2}, \frac{1}{2})$. We have therefore augmented the type-X

---

[*] nabarunc@iitk.res.in

[1] Some studies addressing the same problem using additional fermionic content over and above the type-X 2HDM are [35,36].

2HDM with an additional scalar $SU(2)_L$ doublet. An extra $\mathbb{Z}_2'$ is imposed under which the new doublet is odd while all other fields are even. This addition can be deemed natural since the number of scalar doublets cannot be limited by the electroweak ρ parameter or other fundamental constraints. While the $\mathbb{Z}_2$ is allowed to be broken by the scalar potential, the $\mathbb{Z}_2'$ is exact and therefore disallows mixing between the third doublet with the first two. The third doublet thus remains inert. We refer to this scenario as $(2+1)$HDM and is therefore a generalization of the popular inert doublet model (IDM) [37]. The $(2+1)$HDM has generated some interest in the past. Reference [38] studied in detail the constraints on this scenario from perturbative unitarity and oblique corrections. Reference [39] computed the strength of the $H^\pm W^\mp Z(\gamma)$ vertex at one loop with a particular emphasis of the contribution coming from the inert doublet. A more recent study is [40] that computed various mono-object signals that arise as predictions of the model.

In this work, we compute in detail the two-loop BZ contributions to Δa_μ stemming from the inert doublet. More precisely, we can expect sizeable contributions from such loops owing to the possibility of large scalar trilinear couplings involving the inert scalars. We fold in all relevant theoretical and experimental constraints in the process including dark matter direct detection. Our aim is to see if the $(2+1)$HDM can expand the parameter region in the M_A- $\tan\beta$ plane that is compliant with the muon $g-2$ excess.

The $(2+1)$HDM also predicts an interesting collider signal. The CP-even and CP-odd components of the inert doublet can be pair produced at the LHC with following which odd component can decay to the even component and A. Since the A in this scenario can be potentially heavier than one in the type-X 2HDM and still comply with Δa_μ, a $\tau^\pm$ coming from $A \to \tau^+\tau^-$ will accordingly have a higher transverse momentum in comparison to what is seen in the case of the type-X 2HDM. Moreover, the final state will also have a modified missing-transverse energy spectrum due to the presence of inert scalars. In all, such kinematic features of this signal makes the $(2+1)$HDM discernible from the type-X 2HDM. We have performed detailed analyses of the signal and backgrounds in this work using multivariate techniques and estimated the observability at the 14 TeV LHC.

This study is segmented as follows. We introduce the $(2+1)$HDM scenario in Sec. II and elaborate all the constraints in Sec. III. The details of muon $g-2$ calculation can be found in Sec. IV. The collider analysis is given in Sec. V and we conclude in Sec. VI. Various important formulas are relegated to the Appendix.

II. THEORETICAL FRAMEWORK

The 2HDM, which features two scalar doublets ϕ_1, ϕ_2, is augmented by an additional scalar doublet η in this work. A discrete symmetry $\mathbb{Z}_2'$ is introduced under which $\phi_{1,2} \to \phi_{1,2}$ while $\eta \to -\eta$. The most general scalar potential consistent with the gauge and the $\mathbb{Z}_2'$ symmetry then reads

$$V = V_2 + V_4^a + V_4^b, \tag{2a}$$

$$\text{with} \quad V_2 = -m_{11}^2|\phi_1|^2 - m_{22}^2|\phi_2|^2 + m_{12}^2(\phi_1^\dagger\phi_2 + \text{H.c.}) + \mu^2|\eta|^2, \tag{2b}$$

$$\begin{aligned} V_4^{\{\phi_1,\phi_2\}} = {} & \frac{\lambda_1}{2}|\phi_1|^4 + \frac{\lambda_2}{2}|\phi_2|^4 + \lambda_3|\phi_1|^2|\phi_2|^2 + \lambda_4|\phi_1^\dagger\phi_2|^2 + \frac{\lambda_5}{2}[(\phi_1^\dagger\phi_2)^2 + \text{H.c.}] \\ & + \lambda_6[(\phi_1^\dagger\phi_1)(\phi_1^\dagger\phi_2) + \text{H.c.}] + \lambda_7[(\phi_2^\dagger\phi_2)(\phi_1^\dagger\phi_2) + \text{H.c.}], \end{aligned} \tag{2c}$$

$$\begin{aligned} V_4^{\{\phi_1,\phi_2,\eta\}} = {} & \frac{\lambda'}{2}|\eta|^4 + \sum_{i=1,2}\left\{\nu_i|\phi_i|^2|\eta|^2 + \omega_i|\phi_1^\dagger\eta|^2 + \left[\frac{\kappa_i}{2}(\phi_i^\dagger\eta)^2 + \text{H.c.}\right]\right\} \\ & + [\sigma_1|\eta|^2\phi_1^\dagger\phi_2 + \sigma_2\phi_1^\dagger\eta\eta^\dagger\phi_2 + \sigma_3\phi_1^\dagger\eta\phi_2^\dagger\eta + \text{H.c.}]. \end{aligned} \tag{2d}$$

In the above, V_2 combines all the dimension-two terms of the scalar potential. The dimension-four terms involving ϕ_1, ϕ_2 alone are given by $V_4^{\{\phi_1,\phi_2\}}$. Finally, the term $V_4^{\{\phi_1,\phi_2,\eta\}}$ contains dimension-four terms involving all the three scalar doublets. All parameters in the scalar potential are chosen real to avoid CP violation. Following electroweak symmetry breaking, the scalar doublets are parametrized as

$$\Phi_i = \begin{pmatrix} \phi_i^+ \\ \frac{1}{\sqrt{2}}(v_i + h_i + iz_i) \end{pmatrix}, \qquad (i = 1,2), \qquad \eta = \begin{pmatrix} \eta^+ \\ \frac{1}{\sqrt{2}}(\eta_R + i\eta_I) \end{pmatrix}, \tag{3}$$

where $v_{1,2}$ are the vacuum expectation values and $\tan\beta = \frac{v_2}{v_1}$. The noninert particle spectrum in this case is identical with the 2HDM that consists of the neutral CP-even Higgses h, H, a CP-odd Higgs A, and a charged Higgs H^+. The 2×2 mass matrices brought into diagonal forms by the action of the mixing angles α and β. Of these, the scalar h is taken to be the SM-like Higgs with mass 125 GeV. Further details on the 2HDM spectrum are skipped for brevity.

TABLE I. Various Yukawa scale factors for the lepton-specific case.

ξ_u^h	ξ_d^h	ξ_ℓ^h	ξ_u^H	ξ_d^H	ξ_ℓ^H	ξ_u^A	ξ_d^A	ξ_ℓ^A
$\frac{\cos\alpha}{\sin\beta}$	$\frac{\cos\alpha}{\sin\beta}$	$-\frac{\sin\alpha}{\cos\beta}$	$\frac{\sin\alpha}{\sin\beta}$	$\frac{\sin\alpha}{\sin\beta}$	$\frac{\cos\alpha}{\cos\beta}$	$\cot\beta$	$-\cot\beta$	$\tan\beta$

The inert scalars coming from η do not mix with the ones from $\phi_{1,2}$ on account of the $\mathbb{Z}_2'$. The inert mass eigenstates are then η^+, η_R, and η_I that have the following squared masses:

$$m_{\eta^+}^2 = \mu^2 + \frac{1}{2}\{\nu_1 c_\beta^2 + \nu_2 s_\beta^2\}v^2 + \sigma_1 v^2 s_\beta c_\beta, \tag{4a}$$

$$m_{\eta_R}^2 = \mu^2 + \frac{1}{2}\{(\nu_1+\omega_1+\kappa_1)c_\beta^2 + (\nu_2+\omega_2+\kappa_2)s_\beta^2\}v^2 + (\sigma_1+\sigma_2+\sigma_3)v^2 s_\beta c_\beta, \tag{4b}$$

$$m_{\eta_I}^2 = \mu^2 + \frac{1}{2}\{(\nu_1+\omega_1-\kappa_1)c_\beta^2 + (\nu_2+\omega_2-\kappa_2)s_\beta^2\}v^2 + (\sigma_1+\sigma_2-\sigma_3)v^2 s_\beta c_\beta. \tag{4c}$$

As for the Yukawa interactions, we take the type-X (or lepton-specific) Lagrangian where the quarks get their masses from ϕ_2 while the all the leptons do from ϕ_1. The Yukawa Lagrangian can be expressed as

$$-\mathcal{L}_Y = [y_u \overline{Q_L}\tilde{\phi}_2 u_R + y_d \overline{Q_L}\phi_2 d_R + y_\ell \overline{Q_L}\phi_1 \ell_R] + \text{H.c.} \tag{5}$$

The Yukawa interactions in terms of the physical scalars then becomes

$$\mathcal{L}_Y = \sum_{f=u,d,\ell} \frac{m_f}{v}(\xi_\ell^h h\bar{f}f + \xi_f^H H\bar{f}f - i\xi_f^A A\bar{f}\gamma_5 f) + \frac{\sqrt{2}}{v}[m_u\xi_u^A V_{ud}H^+\bar{u}P_L d + m_d\xi_d^A V_{ud}H^+\bar{u}P_R d + m_\ell\xi_\ell^A H^+\overline{\nu_\ell}P_R\ell + \text{H.c.}]. \tag{6}$$

The various ξ_f factors are tabulated in Table I.

III. CONSTRAINTS

A. Theoretical constraints

The scalar potential remains perturbative if $|\lambda| < 4\pi$, $|y| < \sqrt{4\pi}$, where λ and y, respectively, denote a quartic and Yukawa coupling of the theory. Also, the scalar potential remains bounded from below along various directions in field space if the following conditions are satisfied [40–42]:

$$\begin{aligned}
&\lambda_1 > 0, \quad \lambda_2 > 0, \quad \lambda' > 0,\\
&\lambda_3 + \sqrt{\lambda_1\lambda_2} > 0, \quad \lambda_3 + \lambda_4 - |\lambda_5| + \sqrt{\lambda_1\lambda_2} > 0,\\
&\nu_1 + \sqrt{\lambda_1\lambda'} > 0, \quad \nu_1 + \omega_1 - |\kappa_1| + \sqrt{\lambda_1\lambda'} > 0,\\
&\nu_2 + \sqrt{\lambda_2\lambda'} > 0, \quad \nu_2 + \omega_2 - |\kappa_2| + \sqrt{\lambda_2\lambda'} > 0.
\end{aligned} \tag{7}$$

These conditions are derived assuming that the various directions in field space lie in planes spanned by two field axes. A treatment involving more general directions are computationally hefty to implement and are typically less restrictive than the two-field conditions. We have therefore neglected such possibilities in this work.

The framework is also constrained by invoking unitarity of the S matrix. Electroweak equivalence theorem dictates that the tree-level scatterings of longitudinal components of the gauge bosons can be mapped into $2 \to 2$ tree-level scatterings involving the scalars of the theory at high energies [43]. Unitarity demands that the eigenvalues of the matrices formed in the bases of various $2 \to 2$ scalar scattering states must have magnitudes that are bounded from above at 8π. A detailed analysis on unitarity in three-Higgs doublet models was presented in [38]. In this study, we have deduced the scattering matrices for the scalar potential of Eq. (2), which determined the eigenvalues numerically and demanded that their magnitudes do not exceed the stipulated limit of 8π.

B. Higgs signal strengths

The signal strength for the $h \to X$ channel is defined as

$$\mu_X = \frac{\sigma_{pp\to h}}{\sigma_{pp\to h}^{\text{exp}}}\frac{\text{BR}(h\to X)}{\text{BR}^{\text{exp}}(h\to X)}. \tag{8}$$

We adhere to $\alpha = \beta - \frac{\pi}{2}$ in this work (known as the alignment limit in the context of 2HDMs) in which case the couplings of the fermions and gauge bosons to h become equal to the corresponding SM values. In this limit, the predicted values for the Higgs signal strength in the $b\bar{b}, \tau^+\tau^-, W^+W^-, ZZ, gg$ channels become consistent with the measurements at ATLAS and CMS. The only channel that can still deviate in this limit is $\gamma\gamma$ where the presence of the additional charged scalars H^+, η^+ leads to new one-loop contributions in the $h \to \gamma\gamma$ amplitude. One then has

$$M_{h\to\gamma\gamma}^{\text{NP}} = \sum_{\phi^+=H^+,\eta^+} \frac{\lambda_{h\phi^+\phi^-}v}{2m_{\phi^+}^2} A_0\left(\frac{m_h^2}{4m_{\phi^+}^2}\right). \tag{9}$$

The total amplitude and the decay width then become

$$\mathcal{M}_{h\to\gamma\gamma} = \mathcal{M}_{h\to\gamma\gamma}^{\text{SM}} + \mathcal{M}_{h\to\gamma\gamma}^{\text{NP}}, \tag{10}$$

$$\Gamma_{h\to\gamma\gamma} = \frac{G_F\alpha^2 m_h^3}{128\sqrt{2}\pi^3}|\mathcal{M}_{h\to\gamma\gamma}|^2, \tag{11}$$

where G_F is the Fermi constant. The pertinent loop functions are listed here [44,45]:

$$A_0(x) = -\frac{1}{x^2}(x - f(x)), \tag{12a}$$

$$\begin{aligned} \text{with} \quad f(x) &= \arcsin^2(\sqrt{x});\, x \leq 1 \\ &= -\frac{1}{4}\left[\log\frac{1+\sqrt{1-x^{-1}}}{1-\sqrt{1-x^{-1}}} - i\pi\right]^2; \qquad x > 1. \end{aligned} \tag{12b}$$

The charged scalars do not modify the production cross section of h and the modification to the total width is tiny. The signal strength in the $\gamma\gamma$ channel is then

$$\mu_{\gamma\gamma} \simeq \frac{\Gamma_{h\to\gamma\gamma}}{\Gamma^{\text{exp}}_{h\to\gamma\gamma}}. \tag{13}$$

The latest 13 TeV results on the diphoton signal strength from the LHC read $\mu_{\gamma\gamma} = 0.99^{+0.14}_{-0.14}$ (ATLAS [46]) and $\mu_{\gamma\gamma} = 1.18^{+0.17}_{-0.14}$ (CMS [47]). Upon using the standard combination of signal strengths and uncertainties, we obtain $\mu_{\gamma\gamma} = 1.06 \pm 0.1$ and impose this constraint at 2σ.

The branching ratio of Higgs to invisible states faces upper limits from the LHC. The most recent constraint is $\text{BR}(h \to \text{invisible}) < 18\%$ [48]. We have implemented this constraint in our analysis.

C. Oblique parameters

The NP corrections induced to the oblique parameters [49] in this setup are can be split into a contribution coming from the active doublet (ΔX_{2HDM}) and one from the inert doublet (ΔX_{IDM}).

$$\Delta X = \Delta X_{\text{2HDM}} + \Delta X_{\text{IDM}}, \tag{14}$$

where $X = S,\ T,\ U$. The most constraining for scalar extensions of the SM is the T parameter. The relevant expressions for $\alpha = \beta - \frac{\pi}{2}$ are given here [50]:

$$\begin{aligned} \Delta T_{\text{2HDM}} = \frac{1}{16\pi s_W^2 M_W^2}[F(m^2_{H^+}, m^2_H) \\ + F(m^2_{H^+}, m^2_A) - F(m^2_H, m^2_A)], \end{aligned} \tag{15a}$$

$$\begin{aligned} \Delta T_{\text{IDM}} = \frac{1}{16\pi s_W^2 M_W^2}[F(m^2_{\eta^+}, m^2_{\eta_R}) \\ + F(m^2_{\eta^+}, m^2_{\eta_I}) - F(m^2_{\eta_R}, m^2_{\eta_I})]. \end{aligned} \tag{15b}$$

In the above,

$$\begin{aligned} F(x,y) &= \frac{x+y}{2} - \frac{xy}{x-y}\ln\left(\frac{x}{y}\right) \quad \text{for } x \neq y, \\ &= 0 \quad \text{for } x = y. \end{aligned} \tag{16}$$

The most updated bound reads [11]

$$\Delta T = 0.07 \pm 0.12. \tag{17}$$

We have imposed the stated bound, which has been at 2σ in our analysis.

D. Dark matter

The presence of the inert doublet protected by a discrete symmetry makes its neutral component (η_R or η_I) a DM candidate. The PLANCK collaboration quotes the following as the latest measured value of the DM relic density [51]:

$$\Omega_{\text{Planck}} h^2 = 0.120 \pm 0.001. \tag{18}$$

The other important DM constraint comes from the search of DM-nucleon scattering cross sections by different terrestrial experiments such as XENON-1T [52,53] and PANDA-X [54,55]. The nonobservation of such scatterings has led to upper limits on the DM-nucleon cross section with the most stringent bound for $m_{\text{DM}} < 1$ TeV coming from XENON-1T.

The model is implemented to the publicly available tool microMEGAS [56] in order to compute the relic density and the spin-independent direct detection (SI-DD) cross section. The computed relic density is stipulated to be underabundant in this work as presence of other DM candidates (not accounted for in this work) is assumed. Folding in a 10% experimental error in the measured central value, we demand

$$\Omega h^2 < 0.12 \pm 2 \times 0.012 \tag{19}$$

As for direct detection, we compute the SI-DD cross section σ_{SI} using microMEGAS. We subsequently determine the effective cross section $\sigma^{\text{eff}}_{\text{SI}} = (\frac{\Omega h^2}{\Omega_{\text{Planck}} h^2})\sigma_{\text{SI}}$. This ratio takes care of the fact that the present model accounts for only a part of the observed relic abundance. We add that the SI-DD scatterings in this scenario proceeds via t-channel diagrams involving h and H.

IV. THE MUON $g-2$ AMPLITUDE AND ITS NUMERICAL PREDICTION

We present an elaborate computation of Δa_μ in this section. The electromagnetic interaction of a lepton is given by

$$\bar{\ell}(p_2)\Gamma^\mu \ell(p_1) = \bar{\ell}(p_2)\left[\gamma^\mu F_1(q^2) + \frac{i\sigma^{\mu\nu}q_\nu F_2(q^2)}{2M_\ell}\right]\ell(p_1), \tag{20}$$

with $F_{1,2}(q^2)$ as some form factors. The lepton anomalous magnetic dipole moment is then defined as

$$a_\ell = F_2(0). \tag{21}$$

While giving the expressions for the various Δa_μ contributions in the $(2+1)$HDM, we denote the loop order in the superscript and the particle circulating in the loop in the subscript. The one-loop amplitudes driven by H, A, H^+ in the alignment limit are expressed below:

$$\Delta a_{\mu(H)}^{(1\,\mathrm{loop})} = \frac{M_\mu^2}{8\pi^2 v^2}\left(\frac{M_\mu^2}{M_H^2}\right)(\xi_\mu^H)^2 \int_0^1 dx \frac{x^2(2-x)}{\left(\frac{M_\mu^2}{M_H^2}\right)x^2 - x + 1}, \tag{22a}$$

$$\Delta a_{\mu(A)}^{(1\,\mathrm{loop})} = -\frac{M_\mu^2}{8\pi^2 v^2}\left(\frac{M_\mu^2}{M_A^2}\right)(\xi_\mu^A)^2 \int_0^1 dx \frac{x^3}{(\frac{M_\mu^2}{M_A^2})x^2 - x + 1}, \tag{22b}$$

$$\Delta a_{\mu(H^+)}^{(1\,\mathrm{loop})} = \frac{M_\mu^2}{8\pi^2 v^2}\left(\frac{M_\mu^2}{M_{H^+}^2}\right)(\xi_\mu^A)^2 \int_0^1 dx \frac{x^2(1-x)}{\left(\frac{M_\mu^2}{M_{H^+}^2}\right)x(1-x) - x}. \tag{22c}$$

One notes that $\Delta a_{\mu(H^+)}^{(1l)} < 0$. The corresponding diagrams are shown in Fig. 1.

The two-loop BZ contributions arise upon embedding $h\gamma\gamma, H\gamma\gamma, A\gamma\gamma$, and $H^+W^-\gamma$ form factors that themselves arise at one loop, in a one-loop amplitude. The resulting topology is thus two loop. We first list out the Feynman graphs that feature fermions in the one-loop form factors in Fig. 2.

$$\Delta a_{\mu\{f,H\gamma\gamma\}}^{(2\,\mathrm{loop})} = \sum_f \frac{\alpha_{\mathrm{em}} M_\mu^2}{4\pi^3 v^2} N_C^f Q_f^2 \xi_f^H \xi_\mu^H \mathcal{F}^{(1)}\left(\frac{M_f^2}{M_H^2}\right), \tag{23a}$$

$$\Delta a_{\mu\{f,A\gamma\gamma\}}^{(2\,\mathrm{loop})} = \sum_f \frac{\alpha_{\mathrm{em}} M_\mu^2}{4\pi^3 v^2} N_C^f Q_f^2 \xi_f^A \xi_\mu^A \tilde{\mathcal{F}}^{(1)}\left(\frac{M_f^2}{M_A^2}\right), \tag{23b}$$

$$\begin{aligned}\Delta a_{\mu\{f,H^+W^-\gamma\}}^{(2\,\mathrm{loop})} = {}& \frac{\alpha_{\mathrm{em}} M_\mu^2 N_t |V_{tb}|^2}{32\pi^3 s_w^2 v^2 (M_{H^+}^2 - M_W^2)} \int_0^1 dx [Q_t x + Q_b(1-x)][\xi_d^A \xi_\mu^A M_b^2 x(1-x) + \xi_u^A \xi_\mu^A M_t^2 x(1+x)] \\ & \times \left[\mathcal{G}\left(\frac{M_t^2}{M_{H^+}^2}, \frac{M_b^2}{M_{H^+}^2}, x\right) - \mathcal{G}\left(\frac{M_t^2}{M_W^2}, \frac{M_b^2}{M_W^2}, x\right)\right].\end{aligned} \tag{23c}$$

Here, $N_C^f = 1(3)$ for leptons (quarks). Further, α_{em} denotes the fine structure constant and $Q_t = 2/3, Q_b = -1/3$. Next to come are the two-loop amplitudes induced by the 2HDM scalars running in the loops as shown in Fig. 3. The corresponding amplitudes for $\alpha = \beta - \frac{\pi}{2}$ are expressed below.

$$\Delta a_{\mu\{H^+,\phi\gamma\gamma\}}^{(2\,\mathrm{loop})} = \sum_{\phi=h,H} \frac{\alpha_{\mathrm{em}} M_\mu^2}{8\pi^3 M_\phi^2} \xi_\mu^\phi \lambda_{\phi H^+ H^-} \mathcal{F}^{(2)}\left(\frac{M_{H^+}^2}{M_\phi^2}\right), \tag{24a}$$

$$\Delta a_{\mu\{H,H^+W^-\gamma\}}^{(2\,\mathrm{loop})} = \frac{\alpha_{\mathrm{em}} M_\mu^2}{64\pi^3 s_w^2 (M_{H^+}^2 - M_W^2)} \xi_\mu^H \lambda_{HH^+H^-} \int_0^1 dx x^2(x-1) \times \left[\mathcal{G}\left(1, \frac{M_H^2}{M_{H^+}^2}, x\right) - \mathcal{G}\left(\frac{M_{H^+}^2}{M_W^2}, \frac{M_H^2}{M_W^2}, x\right)\right]. \tag{24b}$$

Finally, Fig. 4 depicts the contributions stemming from the inert scalars via the $h\gamma\gamma$, $H\gamma\gamma$, and $H^+W^-\gamma$ vertices.

$$\Delta a_{\mu\{\eta^+,\phi\gamma\gamma\}}^{(2\,\mathrm{loop})} = \sum_{\phi=h,H} \frac{\alpha_{\mathrm{em}} M_\mu^2}{8\pi^3 M_\phi^2} \xi_\mu^\phi \lambda_{\phi\eta^+\eta^-} \mathcal{F}^{(2)}\left(\frac{M_{\eta^+}^2}{M_\phi^2}\right), \tag{25a}$$

$$\Delta a_{\mu\{\eta_R,H^+W^-\gamma\}}^{(2\,\mathrm{loop})} = \frac{\alpha_{\mathrm{em}} M_\mu^2}{64\pi^3 s_w^2 (M_{H^+}^2 - M_W^2)} \xi_\mu^A \lambda_{H^+\eta^-\eta_R} \int_0^1 dx x^2(x-1)\left[\mathcal{G}\left(\frac{M_{\eta^+}^2}{M_{H^+}^2}, \frac{M_{\eta_R}^2}{M_{H^+}^2}, x\right) - \mathcal{G}\left(\frac{M_{\eta^+}^2}{M_W^2}, \frac{M_{\eta_R}^2}{M_W^2}, x\right)\right], \tag{25b}$$

$$\Delta a_{\mu\{\eta_I,H^+W^-\gamma\}}^{2\,\mathrm{loop}} = \frac{\alpha_{\mathrm{em}} M_\mu^2}{64\pi^3 s_w^2 (M_{H^+}^2 - M_W^2)} \xi_\mu^A \lambda_{H^+\eta^-\eta_I} \int_0^1 dx x^2(x-1)\left[\mathcal{G}\left(\frac{M_{\eta^+}^2}{M_{H^+}^2}, \frac{M_{\eta_I}^2}{M_{H^+}^2}, x\right) - \mathcal{G}\left(\frac{M_{\eta^+}^2}{M_W^2}, \frac{M_{\eta_I}^2}{M_W^2}, x\right)\right]. \tag{25c}$$

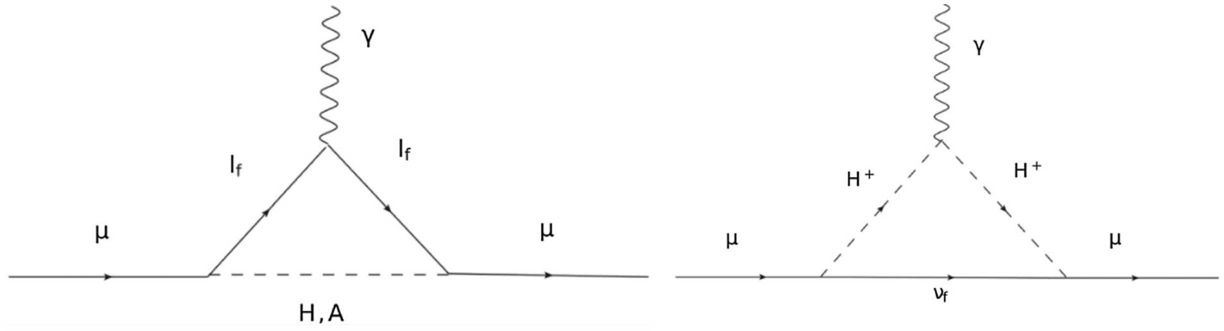

(a) (b)

FIG. 1. One-loop contributions to Δa_μ from (a) H, A, and (b) H^+.

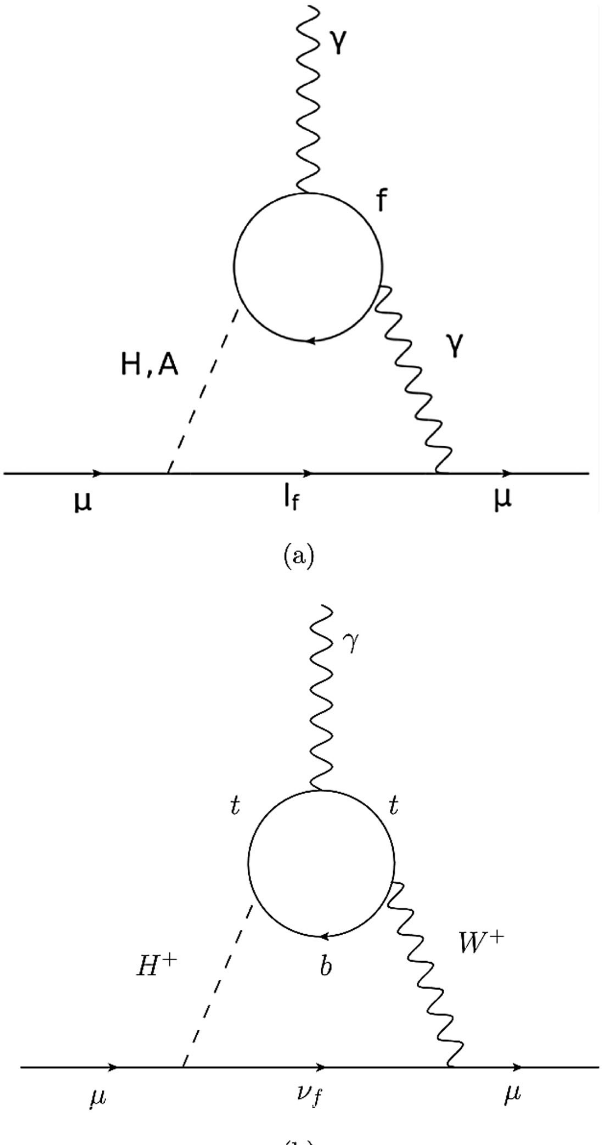

(a)

(b)

FIG. 2. Two-loop contributions to Δa_μ from the fermions through (a) an effective $\phi\gamma\gamma$ vertex and (b) an effective $H^+W^-\gamma$ vertex.

The functions $\mathcal{F}^{(1)}(x)$, $\tilde{\mathcal{F}}^{(1)}(x)$, $\mathcal{F}^{(2)}(x)$, and $\mathcal{G}(a,b,x)$ are expressed in the Appendix. To test the relative magnitudes of the different amplitudes, we compare their numerical values for the reference parameter point $\tan\beta = 50$, $M_H = M_{H^+} = 150$ GeV while varying M_A. We first plot the one-loop contributions and the two-loop BZ contribution $\Delta a_{\mu_{\{f,\phi\gamma\gamma\}}}^{(2\,\mathrm{loop})}$ in Fig. 5. One notes that the A-mediated one-loop amplitude is negative with a sizeable magnitude. In contrast, the two-loop amplitude $\Delta a_{\mu_{\{\tau,A\gamma\gamma\}}}$ is positive. And despite the additional loop suppression, it in fact dominates over the one-loop contribution owing to the $\frac{M_\tau^2}{M_\mu^2}$ enhancement factor. One must remember that though the amplitude involving A and the t-quark implies multiplication by $\frac{M_t^2}{M_\mu^2}$, the same is proportional to $\cot^2\beta$ due to the Yukawa scale factors. Therefore, (A,τ) two-loop amplitude clearly beats the one from (A,t) by a factor $\tan^4\beta\frac{M_\tau^2}{M_t^2} \simeq 650$. An $\sim \mathcal{O}(10^{-9})$ contribution to Δa_μ can therefore be induced for high $\tan\beta$ and low M_A thereby paving way for a resolution of the anomaly. We mention here that the contributions $\Delta a_{\mu_{\{f,H^+W^-\gamma\}}}^{(2\,\mathrm{loop})}$, $\Delta a_{\mu_{\{H^+,\phi\gamma\gamma\}}}^{(2\,\mathrm{loop})}$, and $\Delta a_{\mu_{\{H,H^+W^-\gamma\}}}^{(2\,\mathrm{loop})}$ are suppressed compared to $\Delta a_{\mu_{\{\tau,A\gamma\gamma\}}}$ in the parameter region of interest. More details about the purely 2HDM contribution can be found in [17–24].

The more important component of the present discussion is obviously the contribution coming from the inert sector. The trilinear couplings entering these amplitudes are expressed in the Appendix. Let us examine the trilinear coupling $\lambda_{H\eta^+\eta^-}$ more closely. For $\alpha = \beta - \frac{\pi}{2}$, the dominant behavior is $\lambda_{H\eta^+\eta^-} \simeq \sigma_1(c_\beta^2 - s_\beta^2) \simeq \sigma_1$ for $\tan\beta \gtrsim 20$. Therefore, $\lambda_{H\eta^+\eta^-} \sim \mathcal{O}(1)$ can lead to large values of $\Delta a_{\mu_{\{\eta,H\gamma\gamma\}}}^{(2\,\mathrm{loop})}$. A similar argument reveals that $\lambda_{H^+\eta^-\eta_R}$ and $\lambda_{H^+\eta^-\eta_I}$ can also take sizeable values while $\lambda_{h\eta^+\eta^-}$ remains suppressed for large $\tan\beta$. Of course, the enhanced Yukawa scale factors of the μ lepton with H, A, H^+ also play a role here. We illustrate the strengths of the different $g-2$ amplitudes stemming from the inert scalars in Fig. 6 for

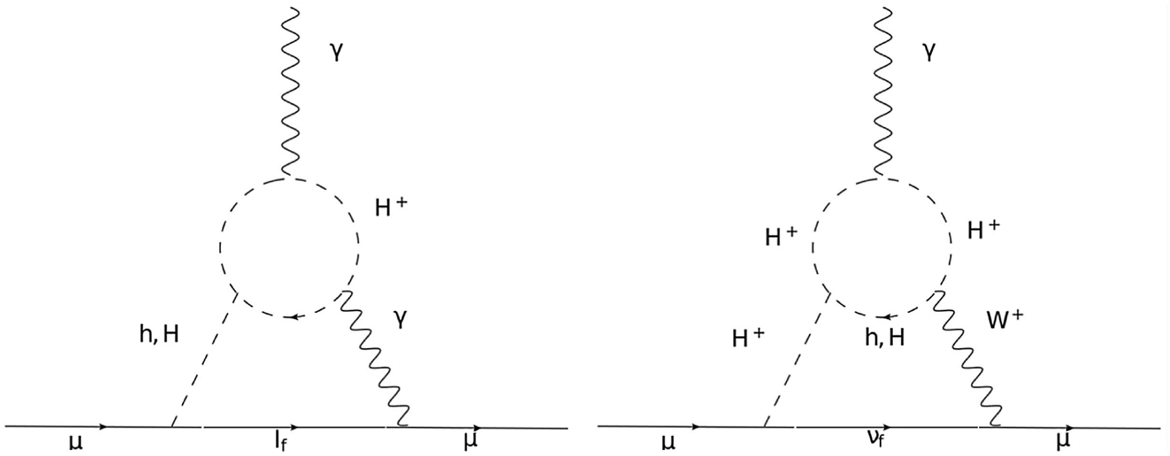

(a) (b)

FIG. 3. Two-loop contributions to Δa_μ from the 2HDM scalars through (a) an effective $\phi\gamma\gamma$ vertex and (b) an effective $H^+W^-\gamma$ vertex.

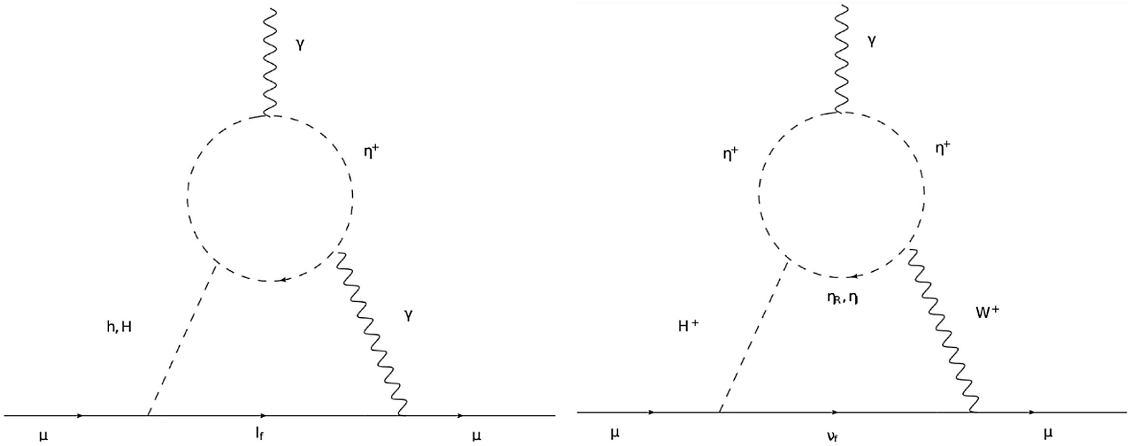

(a) (b)

FIG. 4. Two-loop contributions to Δa_μ from the inert scalars through (a) an effective $\phi\gamma\gamma$ vertex and (b) an effective $H^+W^-\gamma$ vertex.

$M_{\eta_R} = 99$ and 199 GeV. We further fix $M_{\eta^+} = M_{\eta_R} + 1$ GeV and let M_{η_I} vary. The magnitudes of $\lambda_{H\eta^+\eta^-}$, $\lambda_{H^+\eta^-\eta_R}$, and $\lambda_{H^+\eta^-\eta_I}$ are each chosen to be 2π while $\lambda_{h\eta^+\eta^-} = 1$ is taken. The rationale behind such a choice is that trilinear couplings involving H, A, H^+ in one external leg and inert scalars in the other two can attain the maximum strength of 2π while remaining allowed by perturbative unitarity. Taking a common value for these couplings enables a straightforward comparison of the relative magnitudes of the corresponding $g-2$ amplitudes. The largest contributor is the diagram involving the $H\gamma\gamma$ effective vertex. In fact, this amplitude alone adds $\simeq 1.25 \times 10^{-9}$ to the muon magnetic moment when $M_{\eta^+} = 100$ GeV, as seen in Fig. 6(a). An $\mathcal{O}(10^{-10})$ value is also generated for the same M_{η^+} by the diagrams involving the $H^+W^-\gamma$ effective interaction for the shown range of M_{η_I}. The inert sector thus alone suffices to resolve muon $g-2$ at 2σ for $M_{\eta^+} = 100$ GeV. Figure 6(b) shows that the corresponding $g-2$ amplitudes are though expectedly smaller for $M_{\eta^+} = 200$ GeV. In all, the two-loop amplitude driven by the inert scalars is substantial and more importantly, independent of M_A.

We propose a numerical scan to this end to validate the model against the constraints. And this brings us to a counting of the independent model parameters. In the 2HDM sector, m_{11} and m_{22} are eliminated by the tadpole conditions: $\frac{\partial V}{\partial v_1} = \frac{\partial V}{\partial v_2} = 0$. The couplings λ_{1-5} can be expressed in terms of the physical masses, mixing angles, and $\lambda_{6,7}$. In the inert sector, we define the parameters λ_{L_1} and λ_{L_2} below in lines similar to the IDM.

$$\lambda_{L_1} = \nu_1 + \omega_1 + k_1, \tag{26a}$$

$$\lambda_{L_2} = \nu_2 + \omega_2 + k_2. \tag{26b}$$

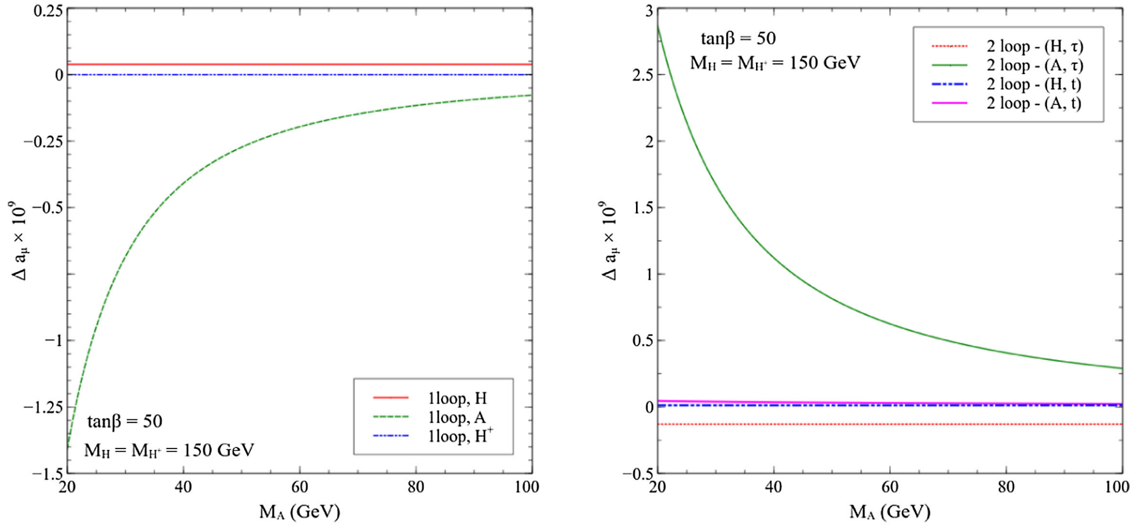

(a) (b)

FIG. 5. One-loop and two-loop fermion-mediated Barr-Zee contributions to Δa_μ. The color coding is explained in the legends.

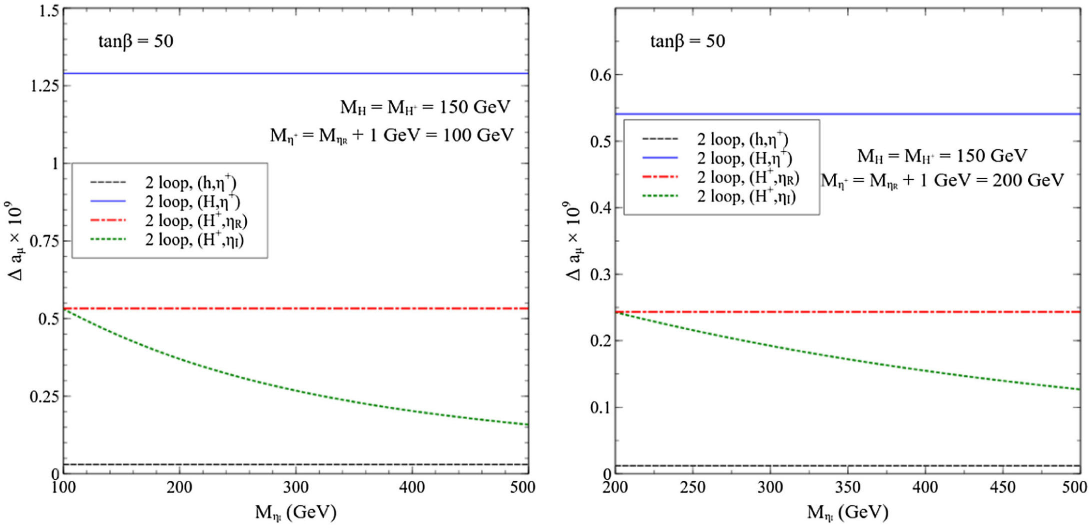

(a) (b)

FIG. 6. Two-loop Barr-Zee amplitudes induced by the inert scalars. The left (right) panel corresponds to $M_{\eta^+} = 100$ GeV (200 GeV). The legends indicate the particles running in the loops. All trilinear couplings involving the inert scalars are chosen to be 2π for illustration.

For insight, the $\eta_R - \eta_R - h$ and $\eta_R - \eta_R - H$ couplings are linear combinations of $\lambda_{L_1} v$ and $\lambda_{L_2} v$ when $\sigma_1, \sigma_2, \sigma_3 = 0$. The parameters $\mu, \omega_2, k_2, \nu_1, \nu_2$ can be traded off using the relations

$$\mu^2 = M_{\eta_R}^2 - \frac{1}{2}\lambda_{L_1} v^2 c_\beta^2 - \frac{1}{2}\lambda_{L_2} v^2 s_\beta^2 - (\sigma_1 + \sigma_2 + \sigma_3) v^2 s_\beta c_\beta, \tag{27a}$$

$$\omega_2 = \frac{M_{\eta_R}^2 + M_{\eta_I}^2 - 2M_{\eta^+}^2 + \omega_1 v^2 c_\beta^2 - 2\sigma_2 v^2 s_\beta c_\beta}{v^2 s_\beta^2}, \tag{27b}$$

$$k_2 = \frac{M_{\eta_R}^2 - M_{\eta_I}^2 - k_1 v^2 c_\beta^2 - 2\sigma_3 v^2 s_\beta c_\beta}{v^2 s_\beta^2}, \tag{27c}$$

$$\nu_1 = \lambda_{L_1} - \omega_1 - k_1, \tag{27d}$$

$$\nu_2 = \lambda_{L_2} - \omega_2 - k_2. \tag{27e}$$

With the alignment limit in place, the independent parameters in the $(2+1)$HDM are therefore $\{m_{12}, M_H, M_A, M_{H^+}, M_{\eta_R}, M_{\eta_I}, M_{\eta^+}, \tan\beta, \lambda_6, \lambda_7, \omega_1, \kappa_1, \sigma_1, \sigma_2, \sigma_3, \lambda_{L_1}, \lambda_{L_2}\}$. We adhere to the same choices for M_H, M_{H^+}, M_{η^+}, M_{η_R} as in the preceding discussion. Additionally, we take $\lambda_6 = \lambda_7 = \lambda_{L_1} = \lambda_{L_2} = 0.01$. The choice of the 2HDM masses is consistent with various exclusion constraints [26] from the LHC on account of the suppressed couplings to quarks in the type-X case. The rest of the parameters are varied as follows:

$$\begin{aligned} &0 < m_{12} < 1\ \text{TeV}, \qquad 20\ \text{GeV} < M_A < 1\ \text{TeV}, \\ &M_{\eta_R} + 1\ \text{GeV} \leq M_{\eta_I} \leq 500\ \text{GeV}, \\ &10 < \tan\beta < 100, \qquad |\omega_1|, \qquad |\kappa_1| < 4\pi, \\ &|\sigma_1|, \qquad |\sigma_2|, \qquad |\sigma_3| < 2\pi. \end{aligned} \tag{28}$$

The (minimum) 1 GeV mass-splitting η_R has with η_I and η^+ disallows W, Z-mediated inelastic direct detection scatterings [57]. Such mass gaps are also consistent with the ΔT constraint. The parameter points passing all the constraints are plotted in the M_A- $\tan\beta$ plane in Figs. 7(a) and 8(a). The most important finding to emerge is that the parameter space compatible with the observed muon $g-2$ excess appreciably expands in the presence of an additional inert scalar doublet. Figure 7(a) shows that an A as heavy as 800 GeV is now allowed for $\tan\beta \simeq 35$ for $M_{\eta^+} = 100$ GeV. This enhancement is clearly attributed to the BZ contributions induced by the inert scalars. Though the enhancement is less in case of $M_{\eta^+} = 200$ GeV, an $M_A = 250$ GeV still complies with Δa_μ for $\tan\beta \simeq 55$ [see Fig. 8(b)].

Figures 7(b) and 8(b) display $\sigma_{\rm SI}^{\rm eff}$ versus $\tan\beta$ for the same parameter points. The $(2+1)$HDM features (co)annihilations mediated by the 2HDM scalars. For instance, $\eta_R\eta_R \to f\bar{f}$ mediated by an s-channel H is an important annihilation channel, where f denotes a SM fermion. This is not encountered in the case where only one active Higgs doublet is present. Since the $M_{\eta^+} - M_{\eta_R} = 1$ GeV in this work, $\eta^+\eta_R \to f\bar{f'}$ and $\eta^+\eta^- \to f\bar{f}$ coannihilations are also triggered mediated by s-channel H^+ and H, respectively. And the most dominant fermionic co (annihilations) are to $\tau\bar{\tau}$ and $\tau\overline{\nu_\tau}$ on account of the $\tan\beta$-enhanced Yukawa interactions. The corresponding co(annihilation) cross sections are thus quite large thereby leading to a small Ωh^2. Consequently, $\sigma_{\rm SI}^{\rm eff}$ remains below the stipulated bound for all the parameter points. This is confirmed by Figs. 7(b) and 8(b). A more detailed discussion of DM phenomenology in the $(2+1)$HDM setup is beyond the scope of this study and can be taken up as a future endeavor.

V. LHC SIGNATURES

We discuss in this section a prospective collider signature of the $(2+1)$HDM framework at the 14 TeV LHC. For $M_A < \frac{M_h}{2}$, a useful channel to look for the A in the pure type-X is $pp \to h \to AA \to \tau^+\tau^-\tau^+\tau^-, \tau^+\tau^-\mu^+\mu^-$ [28,29]. The large h-production cross section through gluon fusion leads to a healthy event rate. However, the primary focus of this work is on a heavier A for which $h \to AA$ is kinematically closed. Hence, the aforementioned channel is not suited to our case. The channel $pp \to H \to AA$, though kinematically open in principle, is also not

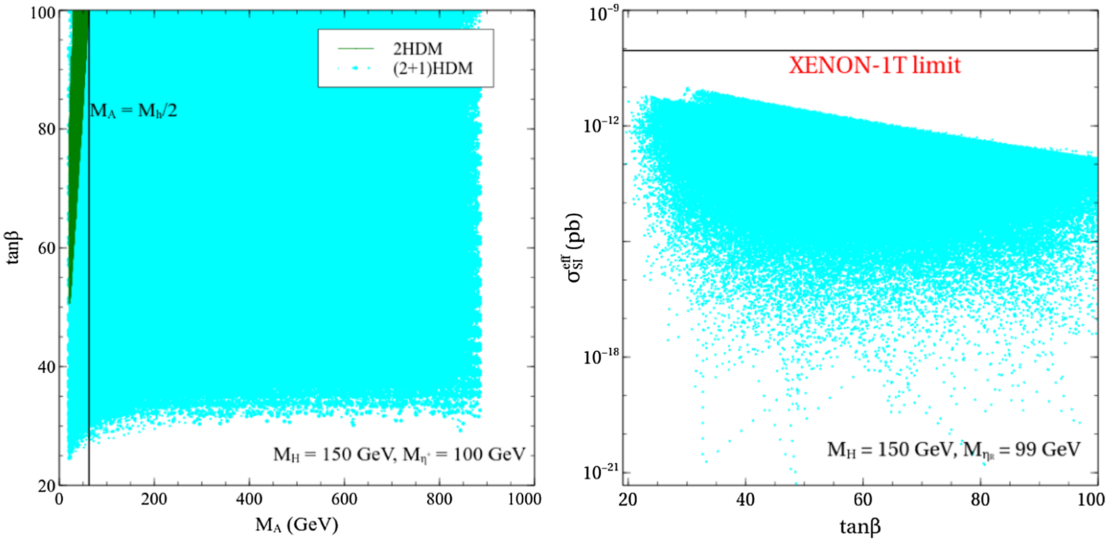

(a) (b)

FIG. 7. (a) Parameter space in the M_A- $\tan\beta$ plane compatible with the observed Δa_μ at 2σ for $M_{\eta^+} = M_{\eta_R} + 1\ \text{GeV} = 100$ GeV. The region to the left of the vertical line is tightly constrained by BR$(h \to AA)$ measurements. (b) Prediction of $\sigma_{\rm SI}^{\rm eff}$ versus $\tan\beta$ for the parameter points in the $(2+1)$HDM compatible with Δa_μ at 2σ for $M_{\eta^+} = M_{\eta_R} + 1\ \text{GeV} = 100$ GeV. The color coding is explained in the legends.

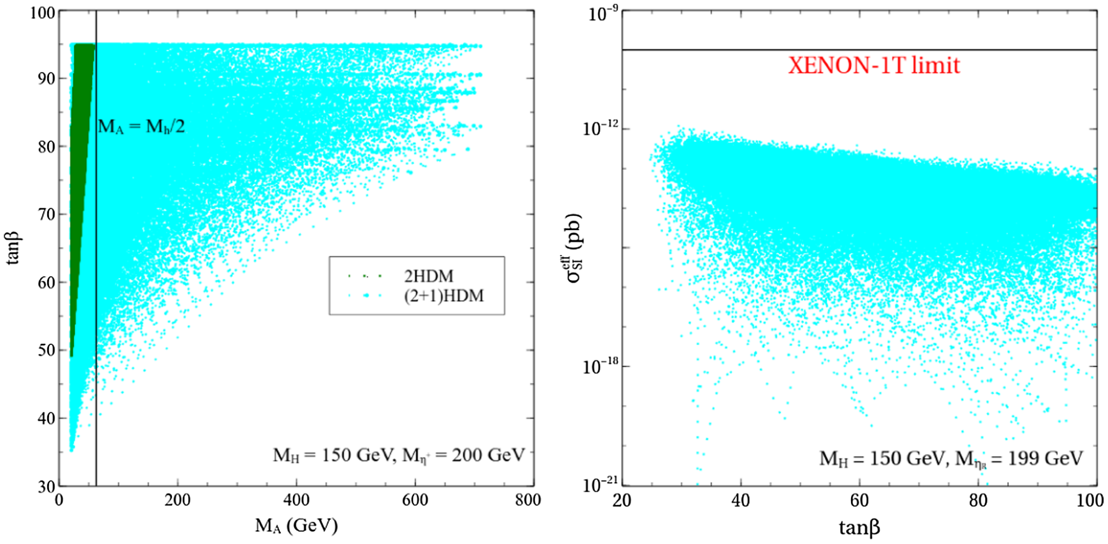

(a) (b)

FIG. 8. (a) Parameter space in the M_A- $\tan\beta$ plane compatible with the observed Δa_μ at 2σ for $M_{\eta^+} = M_{\eta_R} + 1\ \text{GeV} = 200\,\text{GeV}$. The region to the left of the vertical line is tightly constrained by $\text{BR}(h \to AA)$ measurements. (b) Prediction of $\sigma_{\text{SI}}^{\text{eff}}$ versus $\tan\beta$ for the parameter points in the $(2+1)$HDM compatible with Δa_μ at 2σ for $M_{\eta^+} = M_{\eta_R} + 1\ \text{GeV} = 200\,\text{GeV}$. The color coding is explained in the legends.

promising for a couple of reasons. First, this channel mandates $M_H > 2M_A$. Such a heavy H would diminish the relevant BZ amplitudes accordingly. Secondly, the $pp \to H$ production cross section is small owing to the suppressed Yukawa couplings involved here. The selection of LHC signals for the $(2+1)$HDM is guided by the two expectations: (i) the most promising fermionic decay channel is $A \to \tau^+\tau^-$ on account of the enhanced Yukawa coupling. Further, the τ pair will be more boosted in case of an heavier A. (ii) Involving the inert scalars in the signals should ultimately lead to a modified $\not{E}_T$ spectrum with respect to the SM which in turn could be a distinguishing kinematical feature. In view of this, we propose to look at the $pp \to \eta_R\eta_A \to \eta_R\eta_R A \to \tau^+\tau^- + \not{E}_T$ signal. We give the details of the analysis below.

The $\eta_R\eta_I$ pair is dominantly produced via an s-channel exchange of Z. A small contribution also comes from A exchange. Following an $\eta_I \to \eta_R A$ decay, the A subsequently decays to a $\tau^+\tau^-$ pair. The lightest inert scalar η_R registers as missing transverse momentum ($\not{E}_T$). Thus, a modified $\not{E}_T$ spectrum with respect to the SM can be a potential handle to discern the signal from the background. We also look for completely hadronic decays of the τ pair, thereby leading to a $2\tau_h + \not{E}_T$ signature. Instead of a conventional cut-based analysis, we intend to analyse this signal using the more advanced multivariate techniques. A few benchmark points (BPs) are put forth in Table II. The BPs satisfy all the applied constraints and predict the requisite value of Δa_μ, as can be read from Table II. All the three BPs are characterized by $M_{\eta_I} > M_{\eta_R} + M_A$. For these BPs, appropriate values of the quartic couplings ensure that $\eta_I \to \eta_R A$ is the leading decay mode. The subleading one is in fact $\eta_I \to \eta_R Z$. When it comes to the decay of A, it is observed that $A \to ZH, W^\pm H^\mp$ can compete with $A \to \tau^+\tau^-$ for the choice of $M_H = M_{H^+} = 150$ GeV. This is found true especially for BP3. However, the $A \to \tau^+\tau^-$ branching fraction in still $\mathcal{O}(10\%)$ nonetheless.

The relevant interactions of the model have been incorporated in FeynRules [58]. We next discuss the possible background processes. The largest background comes from $pp \to jj + \not{E}_T$ (j denotes a light jet) when both js are misidentified as τ_hs. As the $jj + \not{E}_T$ cross section is $\sim 10^6$ fb, even a small misidentification rate leads to a large $2\tau_h + \not{E}_T$ cross section. Another important background is $pp \to \tau^+\tau^- + \not{E}_T$ that mainly comes from $pp \to W^+W^-, ZZ$ production. Owing to the large $pp \to t\bar{t}$ cross section, the $pp \to t\bar{t} \to \tau^+\tau^- b\bar{b} + \not{E}_T$ process can also lead to a sizeable background when both the b jets are missed. A small contribution also comes from $pp \to W^\pm Z \to \tau^+\tau^-\tau^\pm + \not{E}_T$ when one τ is missed. The cross sections of the signal BPs and the backgrounds are given in Table III. We have used MG5aMC@NLO [59] to generate the signal and background events at the leading order. The CTEQ6L parton distribution function set and default hadronization and factorization scales are used. The parton level events are passed on to PYTHIA8 [60] for showering and hadronization and subsequently to Delphes-3.4.1 [61] for detector simulation. Specifically, we have throughout used the default CMS detector simulation card that comes with Delphes-3.4.1. For an integrated luminosity L, the number in a signal or background sample of events is

TABLE II. BPs used to study the discovery prospects of an A in the $(2+1)$HDM (lepton specific). The values for the rest of the masses are $M_H = M_{H^+} = 150$ GeV, $M_{\eta^+} = M_{\eta_R} + 1$ GeV $= 100$ GeV.

	BP1	BP2	BP3
m_{12}	24.0 GeV	20.4 GeV	21.6 GeV
$\tan\beta$	38.71	53.83	47.98
M_A	206.2 GeV	253.24 GeV	301.26 GeV
M_{η_I}	346 GeV	397 GeV	450.5 GeV
k_1	−0.992743	−2.07345	−0.55292
ω_1	−2.94053	−0.125664	0.13823
σ_1	−5.00142	−5.70513	−6.09469
σ_2	5.7554	−0.263894	1.29434
σ_3	4.05894	5.44124	5.90619
Δa_μ	1.48646	1.51138	1.64289
$\sigma_{\rm SI}^{\rm eff}$	5.28×10^{-48} cm^2	3.81×10^{-50} cm^2	4.42×10^{-49} cm^2
$\mathrm{BR}(\eta_I \to \eta_R A)$	0.844604	0.822958	0.748021
$\mathrm{BR}(A \to \tau^+\tau^-)$	0.99	0.7983	0.341914

TABLE III. Signal and background cross sections at the 14 TeV LHC.

Signal/Backgrounds	Process	Cross section (fb)
Signal		
BP1	$pp \to \eta_R\eta_I \to \eta_R\eta_R A \to \tau^+\tau^- + \not{E}_T$	7.904
BP2		3.867
BP3		0.965
Backgrounds		
	$pp \to jj + \not{E}_T$	1.11×10^6
	$pp \to \tau^+\tau^- + \not{E}_T$	5.80×10^2
	$pp \to t\bar{t} \to b\bar{b}W^+W^- \to \tau^+\tau^- b\bar{b} + \not{E}_T$	8.092×10^3 (next-to-next-to-leading order)
	$pp \to W^\pm Z \to \tau^+\tau^-\tau^\pm + \not{E}_T$	4.31×10^1

determined as $L \times \sigma \times \epsilon$ with σ and ϵ, respectively, referring to the cross section and cut efficiency. The signal significance is computed using the formula $S = \sqrt{2[(N_S+N_B)\log(\frac{N_S+N_B}{N_B}) - N_S]}$ [62], where N_S (N_B) denotes the number of signal (background) events.

Events are selected by demanding exactly two τ_h and zero b jets. Sizeable background fractions are eliminated at this level itself since the background processes in this case mostly lead to flavor-democratic leptons. In addition to this demand, the following trigger-level cuts are also applied:

$$\begin{aligned} &p_T^\ell > 10\ \mathrm{GeV}, \qquad |\eta_{j,\ell}| < 2.5, \\ &\Delta R_{\ell\ell} > 0.2, \qquad \Delta R_{\ell j} > 0.2, \qquad \Delta R_{jj} > 0.4. \end{aligned} \tag{29}$$

In the above, $\Delta R_{mn} = \sqrt{\Delta\eta_{mn}^2 + \Delta\phi_{mn}^2}$ and $\Delta\eta_{mn}, \Delta\phi_{mn}$ are the differences between pseudorapidity and azimuthal angles of mth and nth particles, respectively. In addition, $\ell = e$, μ. It is reminded that light jets come only from showering for the signal and backgrounds for this analysis. We denote the two leading τ-tagged jets by j_1 and j_2 in the decreasing order of their p_T. The following kinematic variables of interest are identified: $p_T^{j_1}$, the transverse momentum of the leading tau jet; $\not{E}_T$, the missing transverse energy; $M_{j_1 j_2}$, invariant mass of the $\tau_h\tau_h$ pair; and $M_{\rm trans}^{\rm vis}$, transverse mass of the $\tau_h\tau_h$ pair. The normalized distributions of these four variables are shown in Figs. 9 and 10. A brief discussion on the kinematic features is in order. The distribution of $p_T^{j_1}$ is shown in Fig. 9(a) for the signal BPs and the backgrounds. The $p_T^{j_1}$ spectrum is seen to be harder in case of the signals than the backgrounds. In fact, the heavier the pseudoscalar, the more boosted are the $\tau_h\tau_h$ pair and hence, the harder is the $p_T^{j_1}$ spectrum. One inspects that the distribution peaks around ≃100, 120, and 120 GeV for BP1, BP2, and BP3, respectively. On the other hand, the backgrounds have their peaks below 100 GeV. Next, Figs. 9(b) and 10(a) show that the spectra of the invariant mass and transverse mass of the $\tau_h\tau_h$ pairs share a correlation. That is, the larger the M_A, the higher is the value where these distributions peak. One must however note that the peak of the $M_{j_1 j_2}$ distribution cannot coincide with M_A on account of the $\not{E}_T$ component in τ decays.

We briefly discuss the sources of $\not{E}_T$ in the signal and backgrounds. In case of the $pp \to W^+W^-, ZZ$

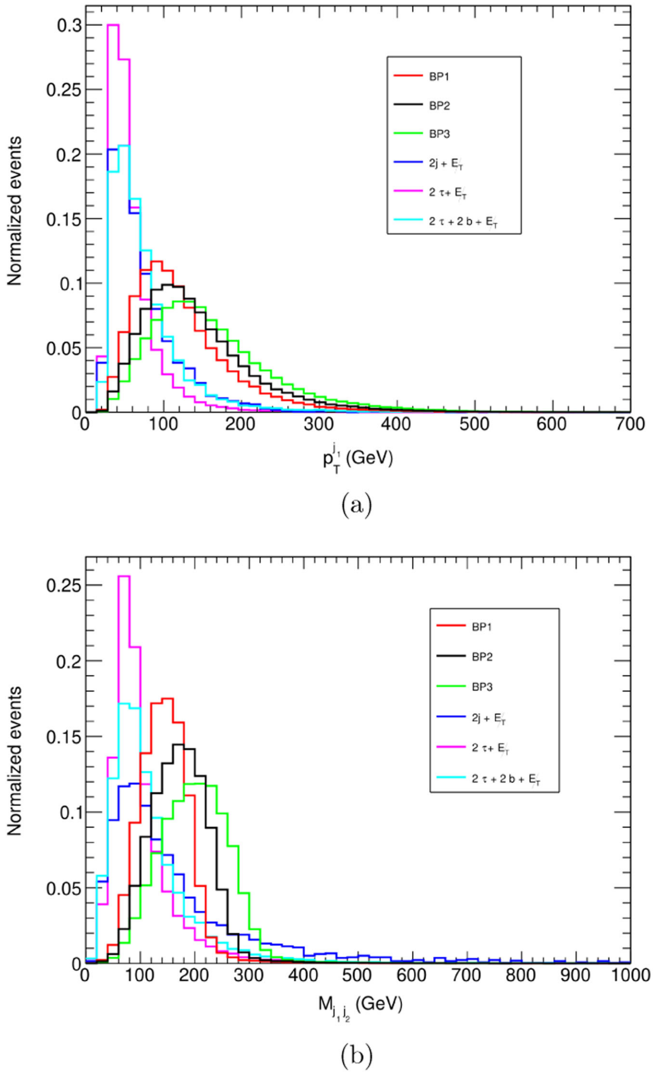

FIG. 9. The distributions of $p_T^{j_1}$ and $M_{j_1 j_2}$ in panels (a) and (b), respectively. The color coding is given in the legends.

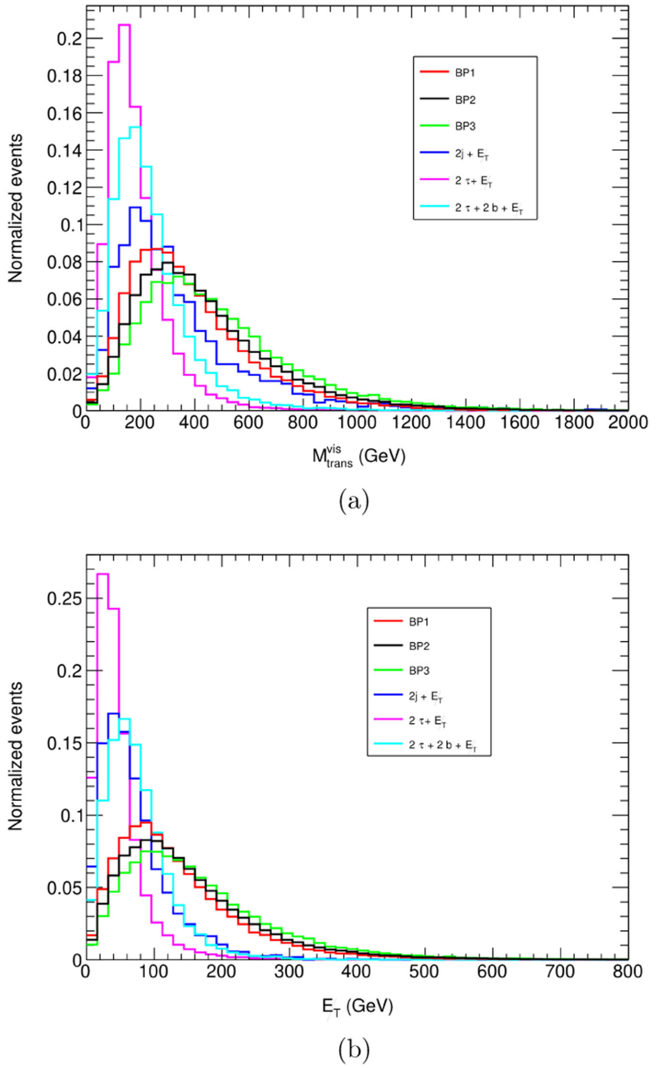

FIG. 10. The distributions of $M_{\mathrm{trans}}^{\mathrm{vis}}$ and $\not{E}_T$ in panels (a) and (b), respectively. The color coding is given in the legends.

backgrounds, for instance, neutrinos coming from $W^{\pm} \to \tau^{\pm}\nu$ and $Z \to \bar{\nu}\nu$ majorly decide the shape of the $\not{E}_T$ distribution. The $pp \to t\bar{t}$ production leads to neutrinos via the $W^{\pm}$ decays. A subleading effect for these backgrounds also comes from the neutrinos emerging from τ decays. In case of the signals, however, the main source of $\not{E}_T$ is in fact the inert scalar η_R. The shape of the $\not{E}_T$ distribution for the signals thus depends on the transverse momentum of η_R. And the masses of η_I and A are such for the BPs that the distribution is harder than the backgrounds. The background distributions all peak below 100 GeV as opposed to the signals that peak at $\gtrsim$100 GeV, as seen in Fig. 10(b).

We now turn to the multivariate analysis using decorrelated boosted decision tree (BDTD) algorithm as implemented within the toolkit for multivariate data analysis (TMVA) [63] framework. A brief overview of the method is as follows. To classify an events as signal-like or backgroundlike, decision trees are used as classifiers. One discriminating kinematic variable with an optimized cut value applied on it is associated with each node of the decision tree, to make the best possible distinction between the signal-like and backgroundlike events. The handle to do this within TMVA is to tune the BDTD variable NCuts. The training of the decision trees starts from a zeroth node and continues till a particular depth specified by the user is reached. This particular depth is termed as MaxDepth. Finally from the final nodes or the leaf nodes, an event can be specified as signal or background according to their purity. An event can be tagged as signal (background) when $p > 0.5$ ($p < 0.5$).

The decision trees are considered weak classifiers as they are prone to statistical fluctuations of the training sample. To circumvent this problem, one can combine a set of weak classifiers into a stronger one and create new decision trees by modifying the weight of the events. This procedure is

TABLE IV. Tuned BDT parameters for BP1, BP2, BP3.

BP	NTREES	MINNODESIZE	MAXDEPTH	NCUTS	KS score for signal (background)	BDT score
BP1	120	2.5	2	55	0.487 (0.035)	0.3521
BP2	150	3	2	40	0.439 (0.016)	0.4047
BP3	120	3	2	50	0.038 (0.105)	0.5336

referred to as boosting. In this analysis, we choose adaptive boost with the input variables transforming in a decorrelated manner, since this is very useful for weak classifiers. It is implemented as decorrelated adaboost in TMVA. To avoid over training of the signal and background samples, the result of the Kolmogorov-Smirnov test, i.e., Kolmogorov-Smirnov (KS) score is demanded to be always >0.01 and stable.

Now the BDTD algorithm orders the kinematic variables that are fed into the algorithm by their importance in discriminating the signal from the background. The following kinematic variables are proposed in this analysis:

$$p_T^{j_1}, p_T^{j_2}, \eta_{j_1}, \eta_{j_2}, \phi_{j_1}, \phi_{j_2},$$
$$\Delta\phi_{j_1\not{E}_T}, \Delta\phi_{j_2\not{E}_T}, \Delta\phi_{j_1j_2}, \Delta\eta_{j_1j_2}, \Delta R_{j_1j_2},$$
$$\not{E}_T, M_{\text{eff}}, p_T^{j_1j_2}, M_{j_1j_2}, M_{\text{trans}}^{\text{vis}}.$$

In the above, $p_T^{j_1j_2}$ straightforwardly refers to the vector transverse momentum of the $\tau_h\tau_h$ system, i.e., $p_T^{j_1j_2} \equiv \sqrt{(p_x^{j_1}+p_x^{j_2})^2+(p_y^{j_1}+p_y^{j_2})^2}$. The variables that turn out to be the most important in BDT ranking are $p_T^{\mu_1}, p_T^{\mu_2}, \eta_{\mu_1}, \eta_{\mu_2}, p_T^{\mu_1\mu_2}, \Delta R_{\mu_1\mu_2}, M_{\text{inv}}^{\mu\mu}, \not{E}_T$. The relevant BDT

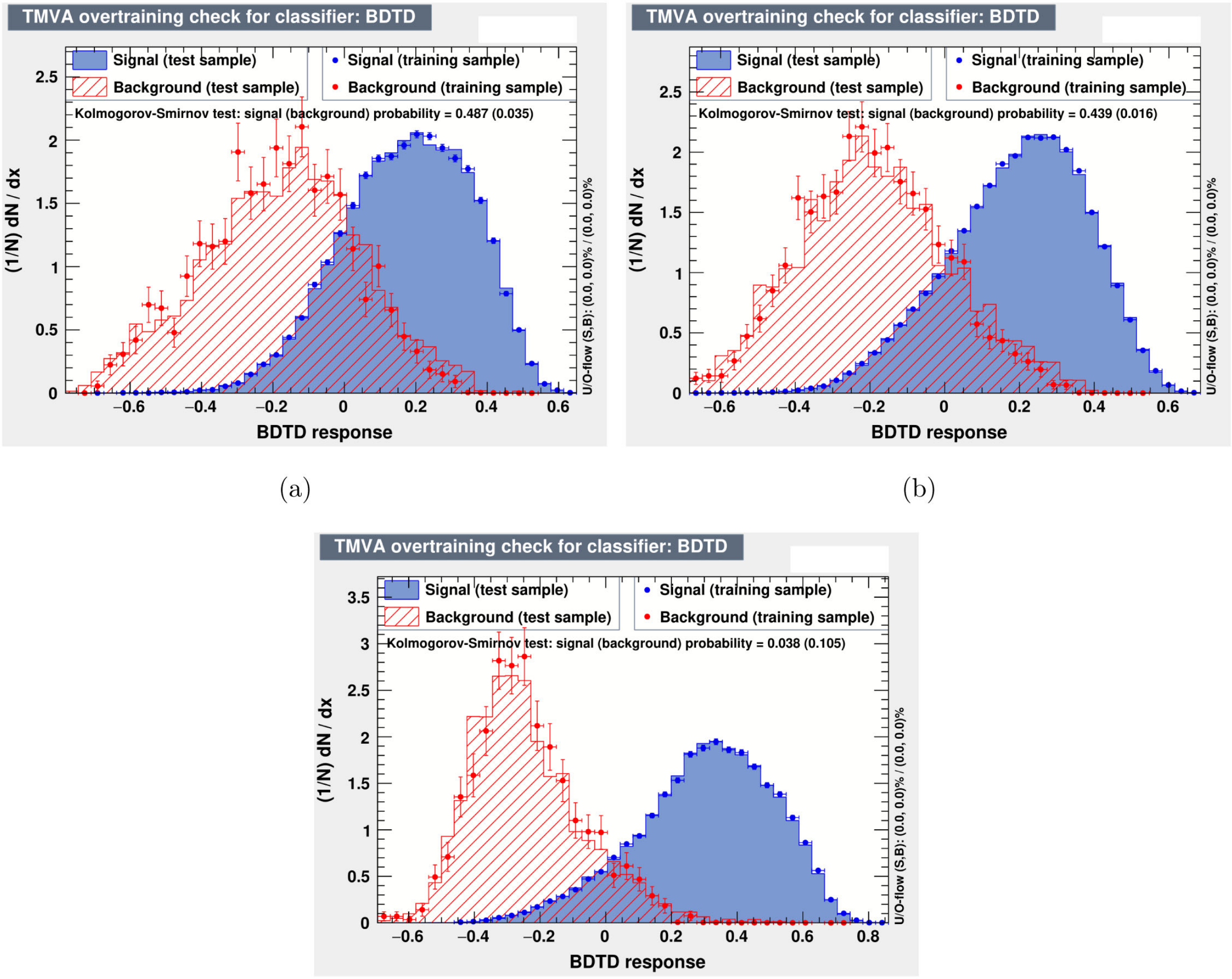

(a)

(b)

(c)

FIG. 11. The KS scores for the chosen lepton-specific benchmarks. The top-left, top-right, and bottom panels correspond to BP1, BP2, and BP3, respectively.

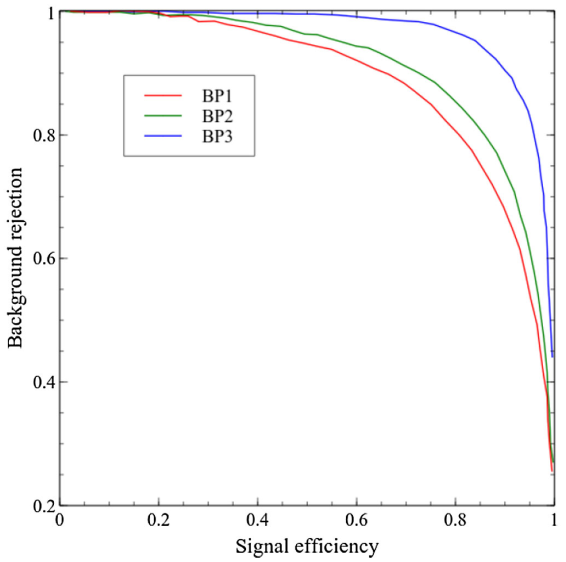

FIG. 12. The receiver's operative characteristic curves for the chosen benchmarks.

parameters are tabulated in Table IV. The signal and background distributions along with their KS scores are depicted in Fig. 11. The degree of background rejection for each BP can be gauged from the receiver's operative characteristic curves as shown in Fig. 12. The efficiency of background rejection is seen to improve sequentially from BP1 to BP3. And this trend is only expected on account of the progressively smaller overlap recorded between the signal BPs and the background upon going from BP1 to BP3, as also concurred by Fig. 11. The yields at an integrated luminosity 3000 fb^{-1} for the signal benchmarks and the backgrounds after optimization through BDTD analysis are given in Table V.

Table V shows that the $jj + \not{E}_T$ background can be hugely reduced and even eliminated through a multivariate analysis. The largest contribution comes from $\tau^+\tau^- b\bar{b} + \not{E}_T$. However the corresponding number of events reduces with the improvement of background rejection as M_A increases. Figure 13 displays the variation of the statistical significance with respect to the integrated luminosity for the BPs. It is seen that a 5σ discovery of a pseudoscalar of mass $\simeq$200 GeV (BP1) is possible at around 1500 fb^{-1} integrated luminosity. BP1 is thus clearly within the discovery reach of the high luminosity Large Hadron Collider (HL-LHC). BP2 requires $\simeq$3200 fb^{-1} for the same indicating that the maximum M_A that can be discovered at 5σ at the HL-LHC is somewhere between 200 and 250 GeV. And BP3 is beyond such a reach.

Therefore, the success of the present analysis lies in predicting a 5σ observability for $M_A \gtrsim 200$ GeV through a $\tau_h\tau_h + \not{E}_T$ signal where the bulk of the missing transverse energy comes from an invisible scalar. In hindsight, $pp \to HA \to \tau^+\tau^-\tau^+\tau^-, \tau^+\tau^-\mu^+\mu^-$ can also be promising in for the scalar mass ranges of interest in this study. While such a

TABLE V. The signal and background yields at 3000 fb^{-1} for BP1, BP2, and BP3 for the $\tau_h\tau_h + \not{E}_T$ channel as obtained from the BDTD analysis.

BP1		
	Process	Yield at 3000 fb^{-1}
Background	$jj + \not{E}_T$	671
	$\tau^+\tau^- + \not{E}_T$	557
	$\tau^+\tau^- b\bar{b} + \not{E}_T$	3276
	$\tau^+\tau^-\tau^\pm + \not{E}_T$	45
	N_B^{BDT}	4548
N_S^{BDT}		481
BP2		
	Process	Yield at 3000 fb^{-1}
Background	$jj + \not{E}_T$	~0
	$\tau^+\tau^- + \not{E}_T$	128
	$\tau^+\tau^- b\bar{b} + \not{E}_T$	1266
	$\tau^+\tau^-\tau^\pm + \not{E}_T$	12
	N_B^{BDT}	1405
N_S^{BDT}		177
BP3		
	Process	Yield at 3000 fb^{-1}
Background	$jj + \not{E}_T$	~0
	$\tau^+\tau^- + \not{E}_T$	21
	$\tau^+\tau^- b\bar{b} + \not{E}_T$	273
	$\tau^+\tau^-\tau^\pm + \not{E}_T$	3
	N_B^{BDT}	297
N_S^{BDT}		19

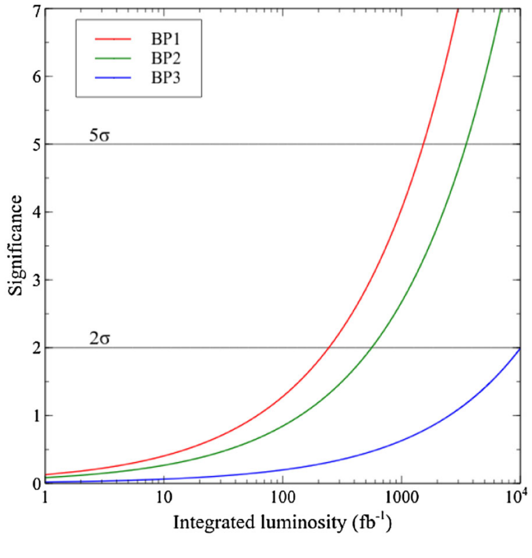

FIG. 13. Variation of the statistical significance with the integrated luminosity.

signal warrants a separate investigation, it remains completely agnostic of the particle sector leading to the requisite Δa_μ even for the heavier A. Therefore, this signal was not analyzed in the present study and can be taken up for further scrutiny in the near future.

VI. CONCLUSIONS

The type-X 2HDM is long known to accommodate the observed excess in muon $g-2$ for high $\tan\beta$ and low M_A. However, nonobservation of $h \to AA$ at the LHC seriously limits the parameter region. We have augmented the type-X 2HDM by an additional inert doublet in this work that is endowed with an additional $\mathbb{Z}_2'$ symmetry. We have taken into account all constraints that are mandated by such a construct and thereafter compute the two-loop Barr-Zee contributions from the inert scalars to Δa_μ. With these additional contributions, we demonstrate that a pesudoscalar mass as large as $M_A \sim 850$ GeV becomes compatible with the observed Δa_μ. The otherwise constrained parameter region in the M_A-$\tan\beta$ plane obtained in case of the standalone 2HDM thus expands to include much higher M_A.

We have probed the scenario at the 14 TeV LHC through the signal $pp \to \eta_R \eta_A \to \eta_R \eta_R A \to \tau^+\tau^- + \not{E}_T$. We have considered a fully hadronic τ pair. Since the τ jets in this case originate from the heavier A, certain kinematic features such as p_T of the leading τ jet and the invariant and transverse masses of the pair are different compared to the SM and even the pure type-X 2HDM. In addition, involvement of the inert scalar in the final state modifies the $\not{E}_T$ spectrum too. We have exploited such a modified kinematics through a multivariate analysis of the signal and backgrounds using the BDTD algorithm. We subsequently predict a 5σ discovery for $M_A \gtrsim 200$ GeV at the HL-LHC.

ACKNOWLEDGMENTS

N. C. acknowledges support from DST, India, under Grant No. IFA19-PH237 (INSPIRE Faculty Award). N. C. thanks Indrani Chakraborty for fruitful discussions on TMVA.

APPENDIX

1. Trilinear couplings

$$\lambda_{h\eta^+\eta^-} = (\sigma_1 c_{\alpha+\beta} - \nu_1 s_\alpha c_\beta + \nu_2 c_\alpha s_\beta), \tag{A1a}$$

$$\lambda_{H\eta^+\eta^-} = (\sigma_1 s_{\alpha+\beta} + \nu_1 c_\alpha c_\beta + \nu_2 s_\alpha s_\beta), \tag{A1b}$$

$$\lambda_{A\eta_R\eta_I} = 2(\sigma_3 c_{2\beta} + (-\kappa_1 + \kappa_2) c_\beta s_\beta), \tag{A1c}$$

$$\lambda_{H^+\eta^-\eta_R} = ((\sigma_2 + \sigma_3) c_{2\beta} + (-\kappa_1 + \kappa_2 - \omega_1 + \omega_2) s_\beta c_\beta), \tag{A1d}$$

$$\lambda_{H^+\eta^-\eta_I} = ((\sigma_2 - \sigma_3) c_{2\beta} + (\kappa_1 - \kappa_2 - \omega_1 + \omega_2) s_\beta c_\beta). \tag{A1e}$$

2. Two-loop functions

$$\mathcal{F}^{(1)}(z) = \frac{z}{2}\int_0^1 dx \frac{2x(1-x) - 1}{z - x(1-x)} \ln\left(\frac{z}{x(1-x)}\right), \tag{A2a}$$

$$\tilde{\mathcal{F}}^{(1)}(z) = \frac{z}{2}\int_0^1 dx \frac{1}{z - x(1-x)} \ln\left(\frac{z}{x(1-x)}\right), \tag{A2b}$$

$$\mathcal{F}^{(2)}(z) = \frac{1}{2}\int_0^1 dx \frac{x(1-x)}{z - x(1-x)} \ln\left(\frac{z}{x(1-x)}\right), \tag{A2c}$$

$$\mathcal{G}(z^a, z^b, x) = \frac{\ln\left(\frac{z^a x + z^b(1-x)}{x(1-x)}\right)}{x(1-x) - z^a x - z^b(1-x)}. \tag{A2d}$$

[1] T. Blum, A. Denig, I. Logashenko, E. de Rafael, B. L. Roberts, T. Teubner, and G. Venanzoni, arXiv:1311.2198.

[2] T. Blum, P. A. Boyle, V. Gülpers, T. Izubuchi, L. Jin, C. Jung, A. Jüttner, C. Lehner, A. Portelli, and J. T. Tsang (RBC, UKQCD Collaborations), Phys. Rev. Lett. **121**, 022003 (2018).

[3] A. Keshavarzi, D. Nomura, and T. Teubner, Phys. Rev. D **97**, 114025 (2018).

[4] M. Davier, A. Hoecker, B. Malaescu, and Z. Zhang, Eur. Phys. J. C **80**, 241 (2020); **80**, 410(E) (2020).

[5] T. Aoyama *et al.*, Phys. Rep. **887**, 1 (2020).

[6] G. Colangelo, M. Hoferichter, and P. Stoffer, J. High Energy Phys. 02 (2019) 006.

[7] M. Hoferichter, B.-L. Hoid, and B. Kubis, J. High Energy Phys. 08 (2019) 137.

[8] K. Melnikov and A. Vainshtein, Phys. Rev. D **70**, 113006 (2004).

[9] M. Hoferichter, B.-L. Hoid, B. Kubis, S. Leupold, and S. P. Schneider, J. High Energy Phys. 10 (2018) 141.

[10] T. Blum, N. Christ, M. Hayakawa, T. Izubuchi, L. Jin, C. Jung, and C. Lehner, Phys. Rev. Lett. **124**, 132002 (2020).

[11] P. A. Zyla *et al.* (Particle Data Group), Prog. Theor. Exp. Phys. **2020**, 083C01 (2020).
[12] G. W. Bennett *et al.* (Muon $g-2$ Collaboration), Phys. Rev. D **73**, 072003 (2006).
[13] B. Abi *et al.* (Muon $g-2$ Collaboration), Phys. Rev. Lett. **126**, 141801 (2021).
[14] T. Albahri *et al.* (Muon $g-2$ Collaboration), Phys. Rev. D **103**, 072002 (2021).
[15] N. G. Deshpande and E. Ma, Phys. Rev. D **18**, 2574 (1978).
[16] G. C. Branco, P. M. Ferreira, L. Lavoura, M. N. Rebelo, M. Sher, and J. P. Silva, Phys. Rep. **516**, 1 (2012).
[17] A. Broggio, E. J. Chun, M. Passera, K. M. Patel, and S. K. Vempati, J. High Energy Phys. 11 (2014) 058.
[18] J. Cao, P. Wan, L. Wu, and J. M. Yang, Phys. Rev. D **80**, 071701 (2009).
[19] L. Wang and X.-F. Han, J. High Energy Phys. 05 (2015) 039.
[20] V. Ilisie, J. High Energy Phys. 04 (2015) 077.
[21] T. Abe, R. Sato, and K. Yagyu, J. High Energy Phys. 07 (2015) 064.
[22] E. J. Chun and J. Kim, J. High Energy Phys. 07 (2016) 110.
[23] A. Cherchiglia, P. Kneschke, D. Stöckinger, and H. Stöckinger-Kim, J. High Energy Phys. 01 (2017) 007; 10 (2021) 242(E).
[24] A. Dey, J. Lahiri, and B. Mukhopadhyaya, Phys. Rev. D **106**, 055023 (2022).
[25] X.-F. Han, T. Li, L. Wang, and Y. Zhang, Phys. Rev. D **99**, 095034 (2019).
[26] D. Chowdhury and O. Eberhardt, J. High Energy Phys. 05 (2018) 161.
[27] A. M. Sirunyan *et al.* (CMS Collaboration), J. High Energy Phys. 11 (2018) 018.
[28] E. J. Chun, S. Dwivedi, T. Mondal, and B. Mukhopadhyaya, Phys. Lett. B **774**, 20 (2017).
[29] E. J. Chun, S. Dwivedi, T. Mondal, B. Mukhopadhyaya, and S. K. Rai, Phys. Rev. D **98**, 075008 (2018).
[30] A. Crivellin, J. Heeck, and P. Stoffer, Phys. Rev. Lett. **116**, 081801 (2016).
[31] S. Iguro, Y. Omura, and M. Takeuchi, J. High Energy Phys. 11 (2019) 130.
[32] A. Jueid, J. Kim, S. Lee, and J. Song, Phys. Rev. D **104**, 095008 (2021).
[33] N. Chen, B. Wang, and C.-Y. Yao, arXiv:2102.05619.
[34] L. Wang, J. M. Yang, M. Zhang, and Y. Zhang, Phys. Lett. B **788**, 519 (2019).
[35] M. Frank and I. Saha, Phys. Rev. D **102**, 115034 (2020).
[36] E. J. Chun and T. Mondal, J. High Energy Phys. 11 (2020) 077.
[37] L. L. Honorez, E. Nezri, J. F. Oliver, and M. H. G. Tytgat, J. Cosmol. Astropart. Phys. 02 (**2007**) 028.
[38] S. Moretti and K. Yagyu, Phys. Rev. D **91**, 055022 (2015).
[39] S. Moretti, D. Rojas, and K. Yagyu, J. High Energy Phys. 08 (2015) 116.
[40] M. Merchand and M. Sher, J. High Energy Phys. 03 (2020) 108.
[41] B. Grzadkowski, O. M. Ogreid, and P. Osland, Phys. Rev. D **80**, 055013 (2009).
[42] F. S. Faro and I. P. Ivanov, Phys. Rev. D **100**, 035038 (2019).
[43] B. W. Lee, C. Quigg, and H. B. Thacker, Phys. Rev. D **16**, 1519 (1977).
[44] A. Djouadi, Phys. Rep. **457**, 1 (2008).
[45] A. Djouadi, Phys. Rep. **459**, 1 (2008).
[46] M. Aaboud *et al.* (ATLAS Collaboration), Phys. Rev. D **98**, 052005 (2018).
[47] A. M. Sirunyan *et al.* (CMS Collaboration), J. High Energy Phys. 11 (2018) 185.
[48] A. Tumasyan *et al.* (CMS Collaboration), Phys. Rev. D **105**, 092007 (2022).
[49] M. E. Peskin and T. Takeuchi, Phys. Rev. D **46**, 381 (1992).
[50] W. Grimus, L. Lavoura, O. M. Ogreid, and P. Osland, Nucl. Phys. **B801**, 81 (2008).
[51] N. Aghanim *et al.* (Planck Collaboration), Astron. Astrophys. **641**, A6 (2020); **652**, C4(E) (2021).
[52] E. Aprile *et al.* (XENON Collaboration), Phys. Rev. Lett. **119**, 181301 (2017).
[53] E. Aprile *et al.* (XENON Collaboration), Phys. Rev. Lett. **121**, 111302 (2018).
[54] A. Tan *et al.* (PandaX-II Collaboration), Phys. Rev. Lett. **117**, 121303 (2016).
[55] X. Cui *et al.* (PandaX-II Collaboration), Phys. Rev. Lett. **119**, 181302 (2017).
[56] G. Bélanger, F. Boudjema, A. Pukhov, and A. Semenov, Comput. Phys. Commun. **192**, 322 (2015).
[57] C. Arina, F.-S. Ling, and M. H. Tytgat, J. Cosmol. Astropart. Phys. 10 (2009) 018.
[58] A. Alloul, N. D. Christensen, C. Degrande, C. Duhr, and B. Fuks, Comput. Phys. Commun. **185**, 2250 (2014).
[59] J. Alwall, R. Frederix, S. Frixione, V. Hirschi, F. Maltoni, O. Mattelaer, H. S. Shao, T. Stelzer, P. Torrielli, and M. Zaro, J. High Energy Phys. 07 (2014) 079.
[60] T. Sjöstrand, S. Ask, J. R. Christiansen, R. Corke, N. Desai, P. Ilten, S. Mrenna, S. Prestel, C. O. Rasmussen, and P. Z. Skands, Comput. Phys. Commun. **191**, 159 (2015).
[61] J. de Favereau, C. Delaere, P. Demin, A. Giammanco, V. Lemaître, A. Mertens, and M. Selvaggi (DELPHES 3 Collaboration), J. High Energy Phys. 02 (2014) 057.
[62] G. Cowan, K. Cranmer, E. Gross, and O. Vitells, Eur. Phys. J. C **71**, 1554 (2011); **73**, 2501(E) (2013).
[63] A. Hoecker *et al.*, arXiv:physics/0703039.
[64] N. Chakrabarty and I. Chakraborty, following paper, Phys. Rev. D **107**, 075013 (2023).